Electronic Supplementary Information for

Polycrystalline SnS_x nanofilm enables CO_2 electroreduction to formate with high current density

Xinzhong Wang[a,†], Shuai Liu[b,†], Hao Zhang[b,†], Shusheng Zhang[c], Ge Meng[d]*, Qian Liu[e], Zhiyong Sun[f]*, Jun Luo[b], and Xijun Liu[g]*

[a] Information Technology Research Institute, Shenzhen Institute of Information Technology, Shenzhen 518172, China

[b] Institute for New Energy Materials and Low-Carbon Technologies, School of Materials Science and Engineering, Tianjin University of Technology, Tianjin 300384, China.

[c] College of Chemistry, Zhengzhou University, Zhengzhou 450000, China.

[d] Key Laboratory of Carbon Materials of Zhejiang Province, College of Chemistry and Materials Engineering, Wenzhou University, Wenzhou 325035, China.

[e] Institute for Advanced Study, Cheng Du University, Chengdu 610106, Sichuan, China.

[h] State Key Laboratory for Marine Corrosion and Protection, Luoyang Ship Material Research Institute (LSMRI), Qingdao 266273, China.

[g] MOE Key Laboratory of New Processing Technology for Non-Ferrous Metals and Materials, and Guangxi Key Laboratory of Processing for Non-Ferrous Metals and Featured Materials, School of Resource, Environments and Materials, Guangxi University, Nanning 530004, China.

† These authors contributed equally to this work.

*E-mail: xjliu@tjut.edu.cn; mengge@wzu.edu.cn; szy_sunrui725@163.com.

Experimental Section

Synthesis of p-SnS_x

The vacuum evaporation method was applied to deposit *p*-SnS_x nanofilm on a piece of gas-diffusion layer (GDL)-modified carbon paper (10 × 10 cm) using a DM-450 vacuum evaporation machine. The SnS_2 slugs (purchased from Alfa Aesar) on a tungsten boat were used as precursors. Before evaporation, the chamber pressure was decreased below 4×10^{-3} Pa using a turbopump. The heating current imposed on the tungsten boat was kept at ~1.5 A, and the evaporation rate was kept at 10 Å s^{-1} during the experiment. The ratio of SnS : SnS_2 can be achieved by adjusting heating current. The thickness of the evaporated film was monitored by a quartz crystal oscillator. The thickness of SnS_x films were kept constant as about 800 nm. The as-obtained carbon paper was directly used as a cathode for CO_2 electrolysis.

Characterizations

The morphologies and microstructures of samples were characterized by scanning electron microscopy (SEM, FEI Verios 460) and transmission electron microscopy (TEM, Talos F200X) equipped with an energy dispersive spectrometer (EDS). Powder X-ray diffraction (XRD) pattern was recorded by an X-ray diffractometer (Rigaku SmartLab 9 kW) at a scan rate of 10 min^{-1} with Cu Kα radiation (λ = 0.154598 nm). X-ray photoelectron spectroscopy (XPS) measurement was collected on a Thermo Scientific K-alpha XPS system with the Al Kα radiation as the X-ray source, and the C 1s peak was referred to the binding energy of 284.8 eV.

ECR performance

ECR tests were first conducted with an electrochemical station (CHI 760E) in an H-type cell with 0.1 M $KHCO_3$ solution. The two compartments were separated by a Nafion membrane. Ag/AgCl and graphite rod were used as the reference and counter electrodes, respectively. Carbon paper coated with the *p*-SnS_x nanofilm (2 cm^2) was used as the working electrode. Prior to the ECR, the cathodic electrolyte was saturated with CO_2/Ar for 30 min, and the rate of CO_2 flow was 20 mL min^{-1}. The linear sweep voltammetry (LSV) curves were recorded at a sweep rate of 10 mV s^{-1}. *i*R compensation was applied to all initial data. All of the potential values were calculated based on the equation: $E_{RHE} = E_{Ag/AgCl} + 0.0591 \times pH + 0.197$. The gaseous products were detected by gas chromatography (Agilent GC-7890). The liquid products were analyzed by ^1H NMR on AVANCE AV III 400 with water peak suppression.

In view of the proportional relationship between ECSA and C_{dl}, the CV test at different scan rates (5, 10, 15, 20, and 25 mV s^{-1}) is performed in a narrow non-Faraday interval (-0.4~-0.35 V vs RHE). The Δj (current difference between anode j_a and cathode current density j_c) corresponding to the intermediate potential is plotted against different scan rates, and the slope of the straight line can reflect the ECSA.

Electrochemical impedance spectroscopy (EIS) was captured using an Autolab PGSTAT302N potentiostat / galvanostat in the frequency range from 10^5 to 10^{-2} Hz with an AC amplitude of 5 mV.

MEA tests

Accoridng to our previous work [17,20], an aqueous MEA cell was assembled using

p-SnS_x as the cathode, and a Ti felt coated with commercial IrO_2 catalyst was applied as the anode. The humidified CO_2 gas was kept at 50 standard cubic centimeter per minute (sccm) during the testing and the anodic electrolyte (0.1 M $KHCO_3$) was circulated. The anode and cathode were physically separated by an anion exchange membrane (AEM).

DFT calculations

DFT calculations use the DMol^3 code for energy calculations of the reaction mechanism. Generalized gradient approximation (GGA) processing is performed using the Perdew-Burke-Ernzerhof (PBE) functional. The {100} facet was used with a 4 x 4 x 4 atom slab and 20 Å between mirror images in the z-axis in the unit cell. Structural and unit cell optimizations were performed with the BFGS algorithm until the maximum cutoff was less than 0.02 eV/atom with the structures being fully optimized. Based on the computational hydrogen electrode model proposed by Nørskov's group, the free energy of species in the electrochemical reaction pathway was calculated.

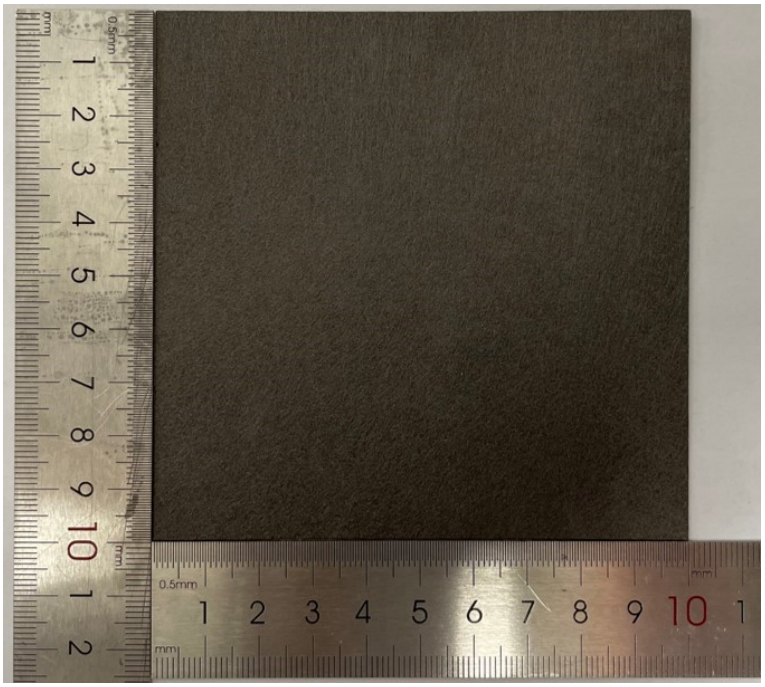

Fig. S1. The optical image of *p*-SnS_x nanofilm coated carbon paper. The

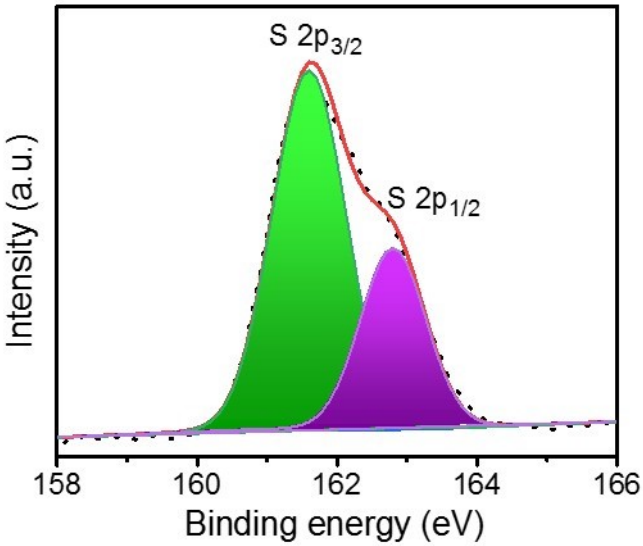

Fig. S2. High-resolution S 2p XPS spectrum of *p*-SnS_x.

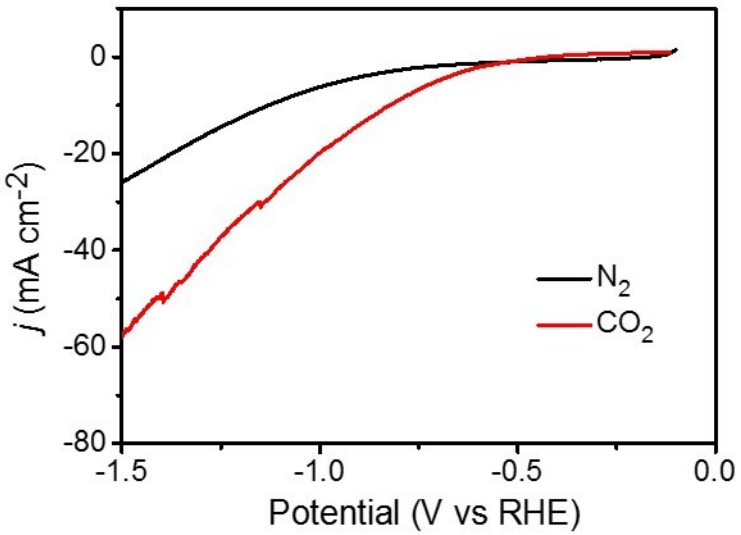

Fig. S3. ECR LSV curves of *p*-SnS_x in Ar-/CO_2-saturated 0.1 M $KHCO_3$ electrolyte.

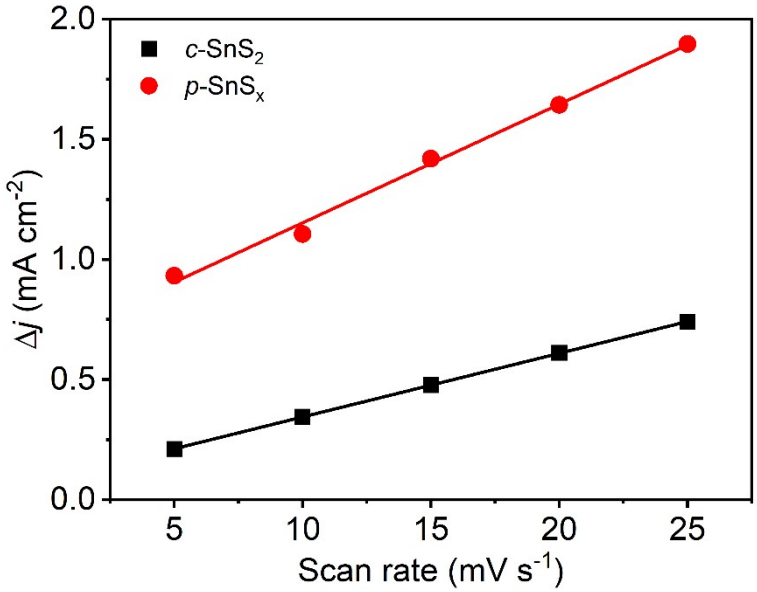

Fig. S4. The double-layer capacitance (C_{dl}) measurements of *p*-SnS_x and *c*-SnS_2 in CO_2-saturated 0.1 M $KHCO_3$ electrolyte. It can be found that *p*-SnS_x delivers a higher C_{dl} (7.8 mF cm^{-2}) than that of *c*-SnS_2 (6.5 mF cm^{-2}), suggesting its remarkably larger number of active sites.

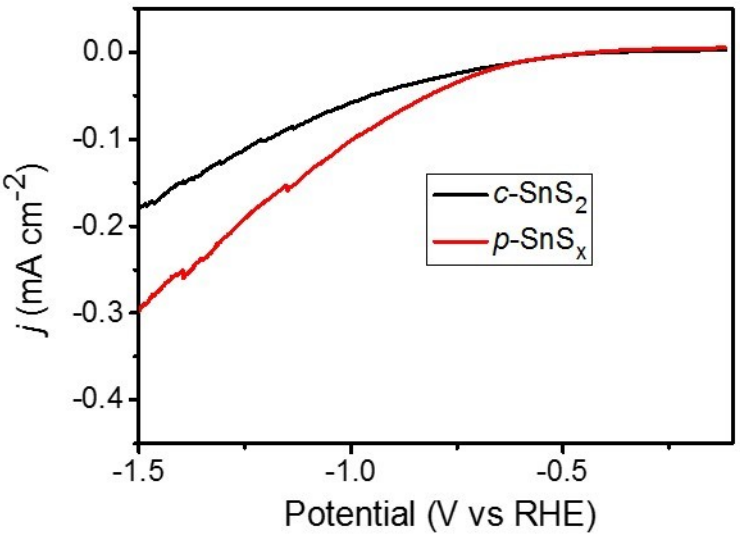

Fig. S5. ECSA-corrected LSV curves of *p*-SnS_x and *c*-SnS_2. Clearly, *p*-SnS_x shows a higher corrected current density than that of *c*-SnS_2.

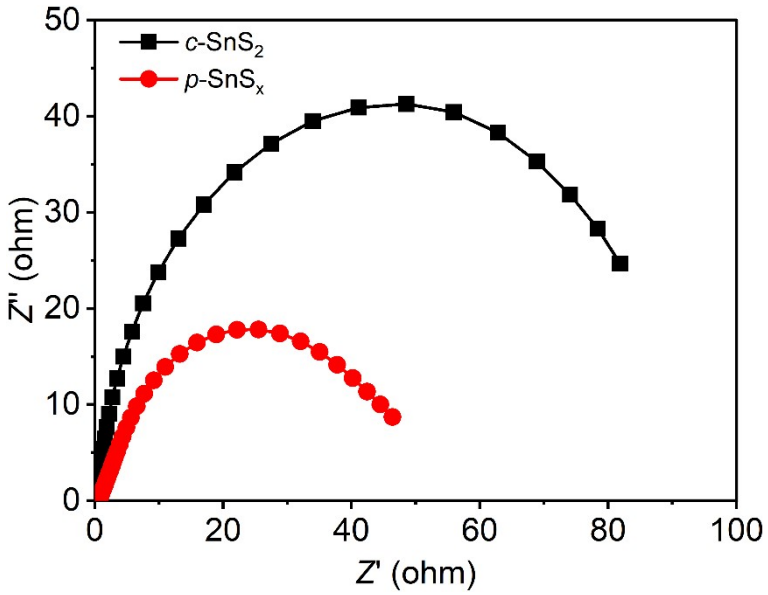

Fig. S6. EIS measurements of *p*-SnS_x and *c*-SnS_2 in CO_2-saturated 0.1 M $KHCO_3$ electrolyte. Clearly, *p*-SnS_x shows a smaller charge transfer resistance as compared to *c*-SnS_2 due to its nanosheets array morphology. This endows fast mass transport and electron transfer rates required for the CO_2 electrolysis.

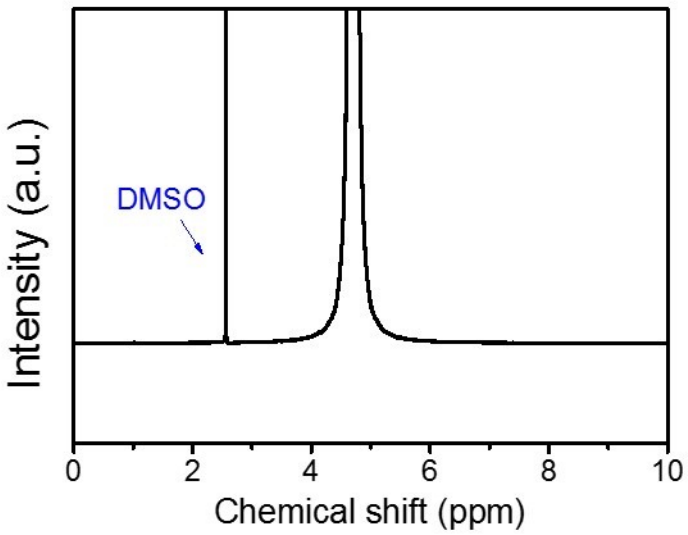

Fig. S7. ^{1}H NMR spectrum of *p*-SnS_x recorded at Ar electrolysis.

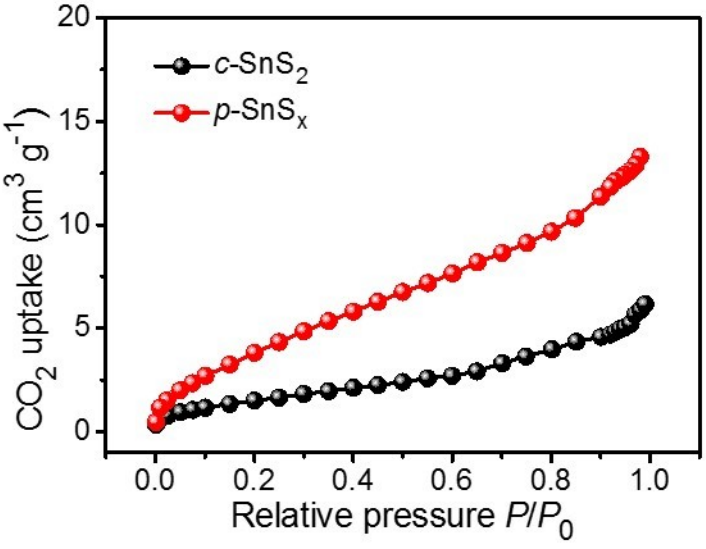

Fig. S8. CO_2 adsorption isotherms of *p*-SnS_x and *c*-SnS_2.

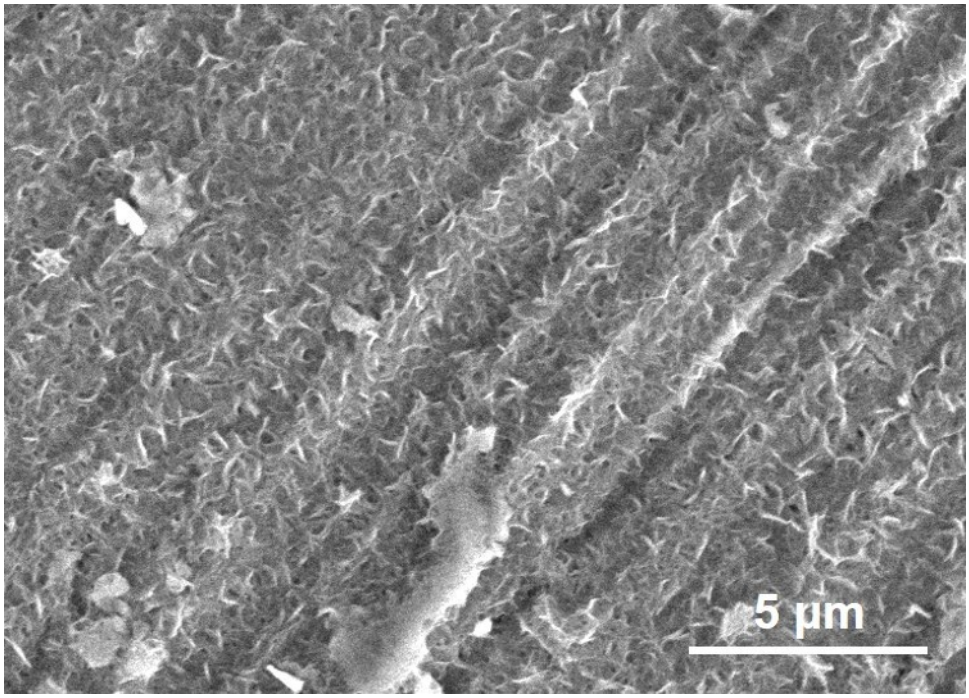

Fig. S9. SEM image of *p*-SnS_x after the CO_2 electrolysis. By contrast, the morphology of *p*-SnS_x still preserved after the long-term electrolysis.

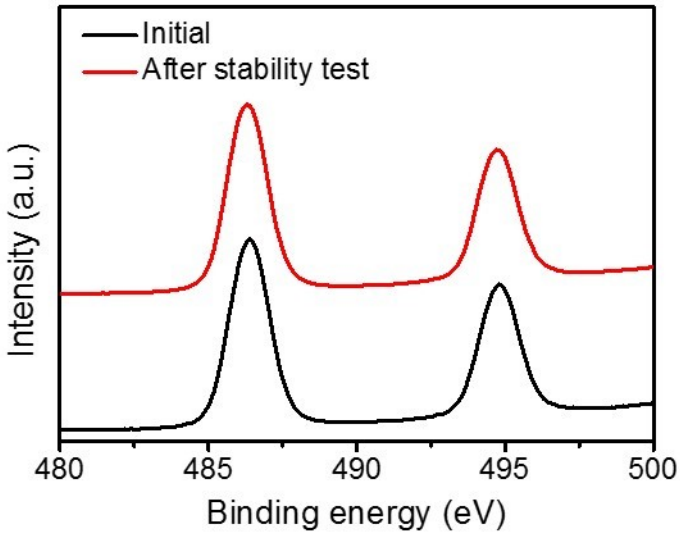

Fig. S10. High-resolution Sn 3d XPS spectrum of *p*-SnS_x after the CO_2 electrolysis.

As seen, there is no notable change before and after the long-term electrolysis, suggesting the good chemical stability of *p*-SnS_x.

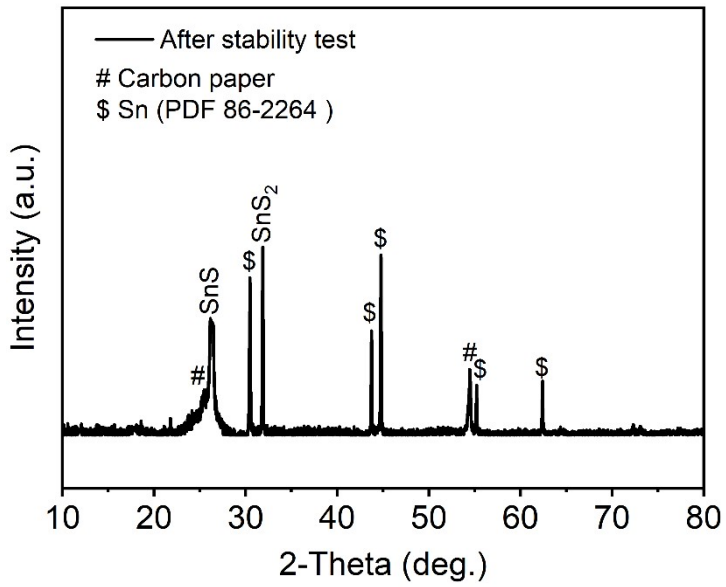

Fig. S11. XRD pattern of *p*-SnS_x after the CO_2 electrolysis. As seen, diffraction peaks correspond to SnS and SnS_2 were still preserved, suggesting *p*-SnS_x is partially reduced at negative working potentials.

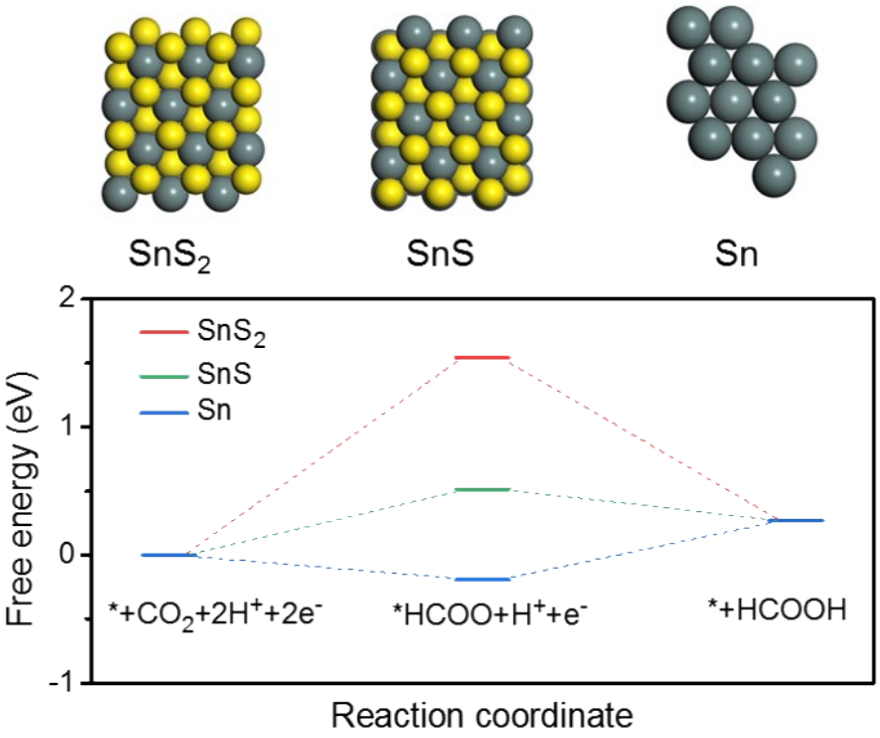

Fig. S12. (a) Geometries of pure Sn, SnS and SnS_2. (b) Free energy diagrams for pure Sn, SnS and SnS_2. It can be found that the formate pathway on pure Sn is more favorable as compared to SnS and SnS_2.

Table S1. Sn-based catalysts of CO_2 electroreduction results tested in H-type cell.

Electrode	Potential	Formate (FE/%)	Stability (h)	Tafel slope (mV dec^{-1})	Current density (mA cm^{-2})	Reference
SnO_2/graphene	−1.8 vs SCE	93%	–	~70	~10 (−1.8 vs SCE)	J. Am. Chem. Soc. 2014, 136, 1734
Sn foil	−1.7 vs SCE	95%	10 (dropped to ~40%)	–	27.9 (−2.0 vs SCE)	J. Electrochem. Soc. 2012, 159, F353
Graphene confined Sn	−1.8 vs SCE	89%	50 (no significant drop)	83	21.1 (−1.8 vs SCE)	Nat. Commun. 2016, 7, 12697
PEI-NCNT/GC	−1.8 vs SCE	87%	~25 (no significant drop)	134	7.2 (−1.8 vs SCE)	J. Am. Chem. Soc. 2014, 136, 7845
SnS_2 derived Sn	−1.4 vs Ag/AgCl	84.5%	~15 (no significant drop)	83	13.9 (−1.4 vs Ag/AgCl)	Nano Energy 2017, 31, 270
Sn-pNW	−0.8 V vs RHE	80%	15 (no significant drop)	134	~10 (−1.0 V vs RHE)	Angew. Chem. 2017, 129, 3699
Sn-SnO_2	−1.2 vs Ag/AgCl	64%	2 (no significant drop)	115	~4 (−1.2 vs Ag/AgCl)	J. Mater. Chem. A 2014, 2, 1647
SnO_2 and Sn nanopowder	−0.6 V vs RHE	67%	5 (dropped to ~50%)	–	~15 (−0.6 V vs RHE)	J. Phys. Chem. C 2015, 119, 4884
Commercial Sn	−1.8 V vs Ag/AgCl	91%	40 (dropped to ~40%)	–	~3 (−1.8 V vs Ag/AgCl)	J. Power Sources 2014, 253, 276
Electrodeposited Sn	−1.4 V vs SCE	91%	6 (dropped to ~35%)	–	15 (−1.4 V vs SCE)	Chem. Eng. J. 2016, 293, 161
SnS_2 monolayers	−0.8 V vs RHE	94 ± 5%	80 (no significant	68	45 (−0.8 V vs	J. Catal. 2018, 364, 125

			drop)		RHE)	
p-SnS_x	−1.0 V vs RHE	97 ± 2%	50 (no significant drop)	79	15 (−1.0 V vs RHE)	*This work*

Table S2. Performance comparison of this work and literature in an AEM-based MEA electrolyzer.

Electrode	**$FE_{formate}$**	**Stability (h)**	**$j_{formate}$ (mA cm^{-2})**	**Reference**
sulfur-doped Sn	>85%	–	25~100	Nat. Commun. 2019, 10, 892
$Bi_{0.1}Sn$	97.8% (−3.6 V)	–	120 (−3.6 V)	Nat. Commun. 2021, 12, 5223
CuBi	98.35 (−1.07 V)	–	56.6 (−1.8 vs SCE)	J. Colloid Interface Sci. 2022, 606, 994
nBuLi-Bi	~95% (−1.44 V)	100	440 (−2.19 vs SCE)	Nat. Commun. 2020, 11, 3633
NRS-SnO	87% (−0.8 V)	–	383 (−0.8 V)	J. CO_2 Util., 2020, 42, 101287
p-SnS_x	93 ± 3% (−2.6 V)	30	420 (−2.6 V)	*This work*